An updated dust-to-star geometry: dust attenuation does not depend on inclination in $1.3 \leq z \leq 2.6$ star-forming galaxies from MOSDEF

Lorenz, B.; Kriek, M.T.; Shapley, A.E.; Reddy, N.A.; Sanders, R.L.; Barro, G.; ... ; Weisz, D.R.

An Updated Dust-to-Star Geometry: Dust Attenuation Does Not Depend on Inclination in 1.3 ⩽ z ⩽ 2.6 Star-forming Galaxies from MOSDEF

Brian Lorenz[1] , Mariska Kriek[2] , Alice E. Shapley[3] , Naveen A. Reddy[4] , Ryan L. Sanders[5] , Guillermo Barro[6] , Alison L. Coil[7] , Bahram Mobasher[4] , Sedona H. Price[8] , Jordan N. Runco[3] , Irene Shivaei[9] , Brian Siana[4] , and Daniel R. Weisz[1]

[1] Department of Astronomy, University of California, Berkeley, CA 94720, USA
[2] Leiden Observatory, Leiden University, P.O. Box 9513, 2300 RA Leiden, The Netherlands
[3] Department of Physics and Astronomy, University of California, Los Angeles, 430 Portola Plaza, Los Angeles, CA 90095, USA
[4] Department of Physics and Astronomy, University of California, Riverside, 900 University Avenue, Riverside, CA 92521, USA
[5] Department of Physics and Astronomy, University of California, Davis, One Shields Avenue, Davis, CA 95616, USA
[6] University of the Pacific, Stockton, CA 90340, USA
[7] Center for Astrophysics and Space Sciences, Department of Physics, University of California, San Diego, 9500 Gilman Drive, La Jolla, CA 92093, USA
[8] Department of Physics and Astronomy and PITT PACC, University of Pittsburgh, Pittsburgh, PA 15260, USA
[9] Steward Observatory, University of Arizona, Tucson, AZ 85721, USA

Abstract

We investigate dust attenuation and its dependence on viewing angle for 308 star-forming galaxies at $1.3 \leqslant z \leqslant 2.6$ from the MOSFIRE Deep Evolution Field survey. We divide galaxies with a detected Hα emission line and coverage of Hβ into eight groups by stellar mass, star formation rate (SFR), and inclination (i.e., axis ratio), and we then stack their spectra. From each stack, we measure the Balmer decrement and gas-phase metallicity, and then we compute the median A_V and UV continuum spectral slope (β). First, we find that none of the dust properties (Balmer decrement, A_V, or β) varies with the axis ratio. Second, both stellar and nebular attenuation increase with increasing galaxy mass, showing little residual dependence on SFR or metallicity. Third, nebular emission is more attenuated than stellar emission, and this difference grows even larger at higher galaxy masses and SFRs. Based on these results, we propose a three-component dust model in which attenuation predominantly occurs in star-forming regions and large, dusty star-forming clumps, with minimal attenuation in the diffuse ISM. In this model, nebular attenuation primarily originates in clumps, while stellar attenuation is dominated by star-forming regions. Clumps become larger and more common with increasing galaxy mass, creating the above mass trends. Finally, we argue that a fixed metal yield naturally leads to mass regulating dust attenuation. Infall of low-metallicity gas increases the SFR and lowers the metallicity, but leaves the dust column density mostly unchanged. We quantify this idea using the Kennicutt–Schmidt and fundamental metallicity relations, showing that galaxy mass is indeed the primary driver of dust attenuation.

Unified Astronomy Thesaurus concepts: Galaxy properties (615); Galaxy evolution (594); High-redshift galaxies (734); Star formation (1569)

1. Introduction

Understanding the effects of dust attenuation on galaxy observations is crucial for accurately determining their physical parameters. Measurements of fundamental parameters such as mass and star formation rate (SFR) may vary significantly depending on the assumed dust properties and distribution (Salim & Narayanan 2020, and references therein). Consequently, it is essential to have a robust understanding of how the effects of dust correlate with various galaxy properties.

A popular model for the for the dust-to-star geometry describes it with two components: dust in the interstellar medium (ISM) that attenuates all light, and more optically thick dust within star-forming regions that primarily affects young stars (e.g., Charlot & Fall 2000). Dust in star-forming regions can be observed through the Balmer decrement, the ratio of the Hα emission-line flux to Hβ. On the other hand, the effects of ISM dust are most apparent from its effect on the shape of the stellar continuum. This two-component model is supported by observations. In particular, Calzetti et al. (2000) found that the dust in nearby starburst galaxies is a combination of a "warm" component (originating from the star-forming regions) and a "cool" component (originating from the ISM) with different optical depths.

However, at higher redshift, there are conflicting results on the effectiveness of the two-component model. For star-forming galaxies at $z \approx 1.4$, Price et al. (2014) find additional dust toward H II regions compared to the stellar attenuation, in agreement with a two-component dust model. Furthermore, the authors find that the difference between the nebular and stellar attenuation decreases with increasing specific SFR (sSFR; SFR/M_*). This result is an additional prediction of the two-component model; as the sSFR decreases, the stellar light is increasingly dominated by stars that are attenuated by the diffuse ISM alone, and thus the observed stellar attenuation decreases relative to the nebular attenuation. In contrast, Reddy et al. (2015) show that for star-forming galaxies at $1.4 \leqslant z \leqslant 2.6$, the difference between the nebular and stellar attenuation increases with SFR. They propose that the nebular lines of galaxies with low SFRs are only attenuated by the dust in the diffuse ISM, while for nebular lines in galaxies with high

SFRs, the attenuation is dominated by highly obscuring dust around star-forming regions. However, this additional dust is patchy and only affects some star-forming regions, so the diffuse ISM component still dominates the stellar attenuation. Consequently, the geometry proposed by Reddy et al. (2015) leads to a large difference in Balmer and stellar attenuation. Hence, these two works at similar redshifts propose different models of the dust-to-star geometry. Other models of the dust-to-star geometry have also been proposed. For example, Reddy et al. (2020) proposed that the youngest brightest stars are most heavily obscured, and Fetherolf et al. (2023) proposed a model in which galaxy mass affects the dust-mixing timescale, and therefore, the attenuation.

Galaxy inclination is a powerful tool for further assessing the dust-to-star geometry at $z \approx 2$. For a simple two-component model (e.g., Charlot & Fall 2000; Price et al. 2014), we expect that the stellar continuum attenuation might vary with the inclination of a disky galaxy because stellar light is expected to pass through more dust in a system that is viewed edge-on. On the other hand, if the obscuration is dominated by dust in the star-forming regions, then the path length does not depend on inclination. In this case, the Balmer decrement would not vary as strongly with inclination. However, for a single dust-component model, or for the low SFR galaxies in the model by Reddy et al. (2015), we would expect the Balmer decrement to increase for more inclined galaxies due to attenuation by ISM dust.

At low redshift, galaxy inclination has proved to be an interesting lens for studying dust properties. In a sample of star-forming disk galaxies at $z \approx 0.07$ from the Sloan Digital Sky Survey (SDSS), Yip et al. (2010) found that the Balmer decrement does not depend on inclination, while the stellar continuum attenuation increases in edge-on galaxies. Additionally, they find that the Balmer-line color excess is higher than the stellar continuum color excess at all inclinations. Both of these results support a two-component model, where the dust affecting the star-forming regions is distributed differently than dust affecting the stellar continuum. This effect is also described in Wild et al. (2011). Along the same lines, Battisti et al. (2017) observed no correlation between Balmer optical depth and inclination for a sample of GALEX star-forming galaxies at $z < 0.105$, but they find a clear correlation between the dust attenuation curve and inclination.

The study of the relation between dust properties and galaxy inclination at $z \approx 2$ to shed light on the observed inconsistencies requires a sample of distant galaxies with measured inclinations and prominent emission lines from which we can derive dust properties. An analysis like this also requires accurate measurements of galaxy parameters such as stellar mass and SFR. Fortunately, by combining the deep spectra from the MOSFIRE Deep Evolution Field survey (Kriek et al. 2015) with photometry and imaging from CANDELS (Grogin et al. 2011; Koekemoer et al. 2011), we now have a sample of high-redshift galaxies for which these detailed dust measurements are possible.

In this work, we use the MOSDEF survey to investigate how dust properties are affected by galaxy inclination, which will improve our understanding of the dust-to-star geometry at $z \approx 2$. In Section 2 we describe the MOSDEF survey and our selection of a subsample for the analysis of dust properties and inclination. In Section 3 we detail our analysis techniques, including spectral stacking and emission-line measurements. In Section 4 we present our findings on the relation between the measured dust properties (Balmer decrement, A_V, and β) and the axis ratios of galaxies. Finally, in Section 5, we propose a three-component dust model that explains our results.

Throughout this work, we assume a ΛCDM cosmology with $\Omega_m = 0.3$, $\Omega_\Lambda = 0.7$, and $H_0 = 70$ km s^{-1} Mpc^{-1}.

2. Data

2.1. The MOSDEF Survey

For this work, we use galaxy spectra from the MOSFIRE Deep Evolution Field (MOSDEF) Survey (Kriek et al. 2015). MOSDEF obtained moderate-resolution ($R = 3000$–3650) rest-frame optical spectra of $\sim$1500 H-band selected galaxies in the CANDELS fields (Grogin et al. 2011; Koekemoer et al. 2011). Observations were taken in the Y, J, H, and K bands using the MOSFIRE spectrograph (McLean et al. 2012) on the Keck I telescope from 2012 December to 2016 May. The sample spans three redshift intervals ($1.37 \leqslant z \leqslant 1.70$, $2.09 \leqslant z \leqslant 2.61$, and $2.95 \leqslant z \leqslant 3.60$), targeted such that many prominent rest-frame emission and absorption features fall into the observed atmospheric transmission windows. For complete details of the MOSDEF survey, including sample selection, observation details, data reduction, and initial properties, we refer to Kriek et al. (2015).

We aim to study the effects of galaxy inclination on the dust parameters, so we need robust axis ratio measurements. The structural parameters for all galaxies in MOSDEF, including axis ratio (b/a), were measured by van der Wel et al. (2012) using GALFIT (Peng et al. 2010). Fits were made to HST imaging in three bands (F125W, F140W, and F160W) from CANDELS (Faber 2011).

In addition to spectra from MOSDEF, we have access to deep photometry from the 3D-HST survey (Brammer et al. 2012; Skelton et al. 2014; Momcheva et al. 2016). Stellar masses are determined by fitting the emission-line-corrected multiband photometry (0.3–8.0 μm) using the FAST fitting code (Kriek et al. 2009). We adopt flexible stellar population models (FSPS; Conroy et al. 2009; Conroy & Gunn 2010), MOSFIRE spectroscopic redshifts, a Chabrier stellar initial mass function (IMF; Chabrier 2003), the Calzetti et al. (2000) attenuation curve, delayed exponentially declining star formation histories, and solar metallicity. These best-fit models also yield measurements of the dust attenuation in the V band (A_V) and UV slope (β).

Prominent emission lines (Hα, Hβ, [O III], [N II], and [O II]) from MOSDEF spectra were fit to determine individual galaxy properties such as SFR and metallicity. Most emission lines were measured by fitting Gaussian and linear components (Kriek et al. 2015; Reddy et al. 2015). For the Balmer lines, stellar absorption must be modeled to ensure accurate flux measurements, so the best-fit stellar population models are used to measure the Balmer absorption lines and correct for the Balmer emission. For the full details on the emission-line fits to the individual galaxies, we refer to Reddy et al. (2015).

2.2. SFR Measurement

For our analysis, it is important to have an accurate SFR measurement for all galaxies in our sample. All galaxies in MOSDEF that have a strong (3σ) detection in Hα and Hβ have a measured dust-corrected SFR (Reddy et al. 2015; Shivaei et al. 2015). In summary, the measured Hα flux is dust-
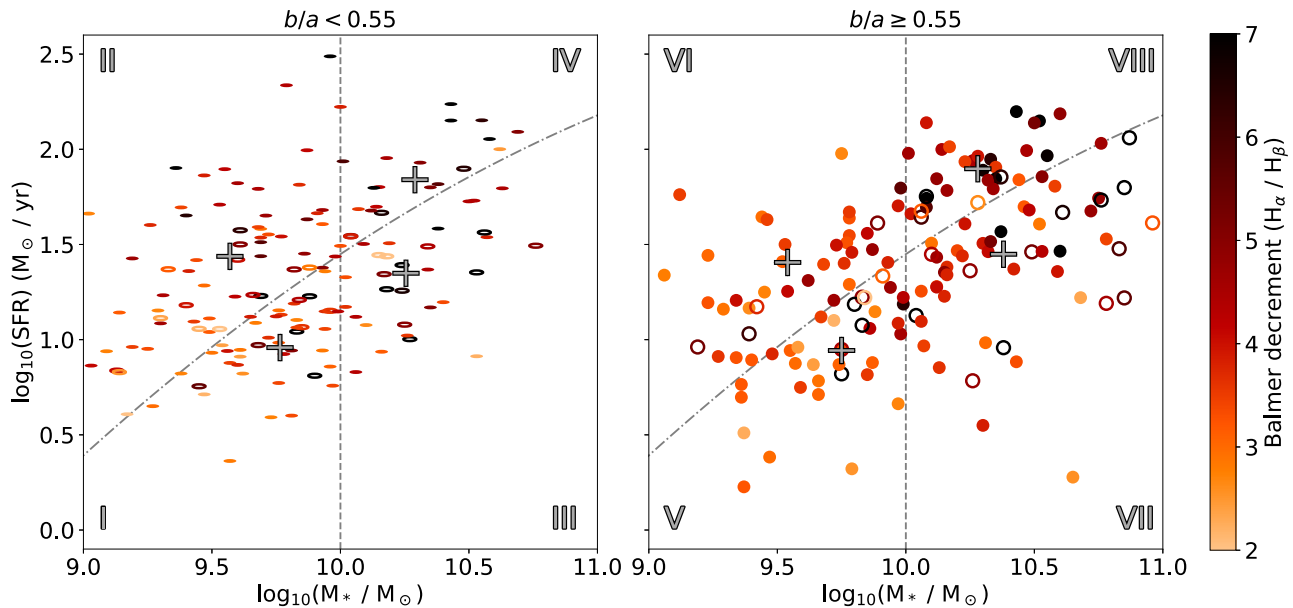
Figure 1. SFR vs. stellar mass of star-forming galaxies in our subsample from the MOSDEF survey at $1.37 \leqslant z \leqslant 2.61$, split into edge-on galaxies ($b/a < 0.55$) (left, ellipses) and face-on galaxies ($b/a \geqslant 0.55$) (right, circles). These symbols are used throughout this work to denote edge-on (ellipses) and face-on (circles). The dashed lines show the divisions into groups by mass and the Whitaker et al. (2014) fit to the star-forming main sequence scaled to our sample. Symbols are color-coded by their initial measurement of Balmer decrement, and galaxies with lower limits on their Balmer decrement are displayed as open points. The median stellar mass and SFR for each of the eight groups is denoted with a gray cross. From this figure, it is already apparent that higher-mass galaxies have higher Balmer decrements.

corrected using the Balmer decrement (Hα/Hβ) and the Cardelli et al. (1989) extinction curve (which was shown to work well for MOSDEF galaxies by Reddy et al. 2020), and it was then converted into the Hα luminosity using the measured redshift. The SFRs are then determined from the Hα luminosity assuming a Chabrier (2003) IMF and the relation from Hao et al. (2011) for solar metallicity. In this work, we adopt these measured SFRs. However, we only include galaxies with at least a 5σ Hα detection for a more robust analysis and measurement of the emission-line properties after stacking (see Section 2.3).

For the galaxies that have a 5σ Hα measurement but no detected Hβ emission, we can only estimate a lower limit on the Balmer decrement using the previous method, and therefore, a lower limit on the SFR. Instead, for these galaxies that lack significant Hβ detections, we estimate the SFR based on Hα alone, correcting for dust using the A_V from the best-fit FAST models. We use a Calzetti et al. (2000) extinction law to correct from the V band at 5500 Å to the wavelength of Hα at 6565 Å. Finally, using the SFR calculation from Hao et al. (2011) and assuming a Chabrier (2003) IMF, we compute the SFR. We performed this calculation for all galaxies in the sample, including the galaxies that had strong Hβ detections. The SFRs measured from both methods agreed well, with an offset of 0.1 dex and similar scatter (see also Price et al. 2014).

2.3. Sample Selection

For this work, we need a complete sample of star-forming galaxies with measured masses, SFRs, and axis ratios. To carry out measurements of the emission features, we require galaxies in our sample to have a detected Hα line and a covered Hβ line. Consequently, we restrict our sample to $1.37 \leqslant z \leqslant 2.61$ so that

the Hα and Hβ emission features are targeted for all galaxies. This reduces the original $\sim$1500 galaxies to 1061.

We then apply the following selection criteria to limit the sample to star-forming galaxies with accurate redshifts, SFRs, and little contamination from other sources. First, we remove any galaxies that do not have a high-quality redshift measurement from MOSDEF because we need to be able to accurately measure the location of the emission features (114 galaxies). Some galaxies do not have coverage of the Hα (43) or Hβ (82) emission lines, which are essential for our measurement of the Balmer decrements. Similarly, galaxies that do not have at least a signal-to-noise ratio of 5 for their Hα measurement are discarded (267). In addition, any galaxies classified as active galactic nuclei (AGN) in MOSDEF are removed (Coil et al. 2015; Azadi et al. 2017), ensuring that any emission lines are almost entirely associated with star formation (144). Next, we remove galaxies with axis ratio measurements that were flagged as suspicious, bad, or nonexistent by GALFIT and for which the differences between the F125W and F160W axis ratios exceed 0.08 (15). We restrict our sample to galaxies with $9 \leqslant \log_{10}(M_*/M_\odot) \leqslant 11$ because the sample is only complete down to a stellar mass of $10^9 M_\odot$ (25). Finally, any galaxy in which Hα or Hβ is contaminated by a sky line is removed, where sky lines are identified by pixels for which the measured error is at least 10 times larger than the median measured error of the spectrum (63). After this process, 308 galaxies remained in our sample. Their masses, SFRs, and Balmer decrements or lower limits are displayed in Figure 1. All remaining galaxies fall in the star-forming region of the UVJ diagram (see Section 4; e.g., Wuyts et al. 2007; Williams et al. 2009).

We note that these selection criteria may introduce some biases into our sample. In particular, we caution that the sample may be missing the most heavily obscured systems because a signal-to-noise ratio of 5 is required for their Hα measurement.
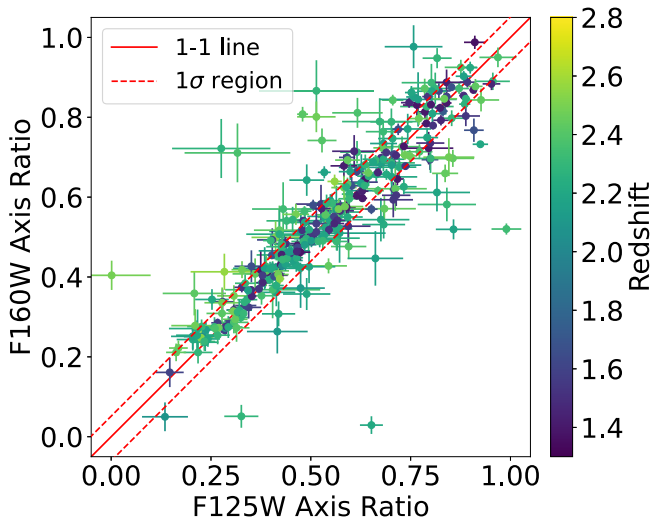
Figure 2. Comparison between the measured F125W and F160W axis ratios for the galaxies in our sample, color-coded by redshift. A one-to-one line is drawn in solid red, and the dashed lines show the 16th and 84th percentiles of the distribution of deviations from the one-to-one line. The measurements are well correlated, so there is very little ambiguity between edge-on and face-on galaxies when they are divided into two axis-ratio groups. We choose to use F160W axis ratios for galaxies in the higher-redshift group ($z > 2.09$) and the F125W axis ratios for galaxies in the lower-redshift group ($z < 1.7$) so that all galaxies are classified at similar rest-frame wavelengths.

2.4. Axis Ratios

To determine the effects of inclination on dust attenuation, we require accurate axis ratio measurements for all galaxies. As mentioned in Section 2.1, axis ratios (b/a) were measured in F125W, F140W, and F160W by van der Wel et al. (2012) using GALFIT (Peng et al. 2010). Due to their higher coverage and signal-to-noise ratio, we limit our analysis to the F125W and F160W axis ratio measurements. We checked the consistency of the F125W and F160W axis ratios, and for the vast majority of galaxies, they are consistent to better than 0.1 (see Figure 2). Therefore, either the F125W or the F160W axis ratio should be a robust way to split the galaxies into groups, as described in Section 3.1. Since the galaxies come from two distinct redshift samples, $1.37 \leqslant z \leqslant 1.70$ and $2.09 \leqslant z \leqslant 2.61$, using only one filter would measure axis ratios at a wide range of rest-frame wavelengths. To better compare the galaxies, we use the F125W axis ratios for the lower-redshift sample (resulting in a median rest wavelength of 4900 Å) and the F160W axis ratios for the higher-redshift sample (resulting in a median rest wavelength of 4700 Å).

2.5. Galaxy Morphology

For our work, we examine galaxy parameters as a function of galaxy inclination. We use the axis ratio as a proxy of galaxy inclination, which assumes that all galaxies are disks. Therefore, we must ensure that the galaxies in our sample are consistent with being disky. Given the axis-ratio distribution of the galaxies, we can infer the properties of the population. As described in Lambas et al. (1992), a randomly oriented distribution of disk galaxies is expected to have a relatively flat distribution of axis ratios, while a randomly oriented distribution of ellipticals will have an increasing distribution that peaks at roughly (b/a) = 0.8. Figure 3 shows the distribution of axis ratios for the galaxies in our sample, which is consistent with the expected distribution for disk galaxies
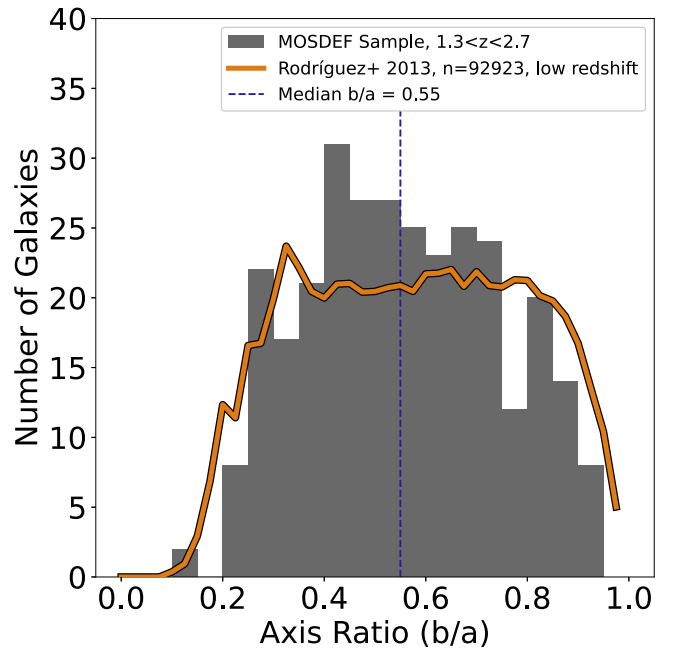
Figure 3. Histogram of the axis ratios for all galaxies in our sample, with a low-redshift star-forming disky comparison sample from Rodríguez & Padilla (2013) in orange. The dashed blue line shows the division between edge-on and face-on galaxies by the median axis ratio ($b/a = 0.55$). The observed distribution is consistent with the expected relatively flat distribution for disk galaxies, and it is inconsistent with the expected rising distribution for elliptical galaxies.

and inconsistent with the expected distribution for elliptical galaxies. Finally, Price et al. (2016, 2020) showed that the star-forming galaxies in MOSDEF at $z \approx 1.5$ and $z \approx 2.2$ have an average v/σ of $\approx$3.5 and $\approx$2.0, respectively, consistent with being rotating disks. Thus, we can assume in this work that galaxies are disky, so the axis ratio is a good indicator of the galaxy inclination.

We also note that at this epoch of peak star formation, galaxy disks are thick (Elmegreen & Elmegreen 2006) and turbulent (Genzel et al. 2008; Simons et al. 2017), unlike the more rotationally supported disks that are observed locally. We further explore the implications of disk morphology as we discuss our results (Section 5.1).

3. Data Analysis

Our goal in this work is to measure the effects of galaxy inclination on the dust attenuation for a complete sample of distant star-forming galaxies. However, many galaxies do not have a detected Hβ line in their spectra, which is necessary to measure the Balmer decrement. By stacking spectra from galaxies with similar properties, we can dramatically increase the signal-to-noise ratio of the spectra and measure emission features, such as Hβ, that were undetected in the individual spectra.

3.1. Forming Groups

Since we require accurate emission-line measurements to determine Balmer decrements, we divide the galaxies into eight groups with similar properties and stack their spectra. Many galaxy properties are known to vary strongly with mass and SFR, such as metallicity, morphology, and kinematics. Therefore, we

ensure that galaxies of similar masses and SFRs are stacked together. For this sample, we divide the SFR-M_* plane into four bins, as shown in Figure 1. In particular, the galaxies are divided by mass into $9 \leqslant \log_{10}(M_*/M_\odot) < 10$ (which we now refer to as "low-mass") and $10 \leqslant \log_{10}(M_*/M_\odot) < 11$ (referred to as "high-mass"). Then, to complete dividing the SFR-M_* plane, we use the star-forming main sequence (SFMS) rather than the SFR alone. The SFMS is a tight relation between the SFR and mass of galaxies that varies with redshift. The position of a galaxy compared to the SFMS is an indicator of how quickly it is forming stars relative to galaxies of similar mass and redshift. We linearly scale the SFMS fit from Whitaker et al. (2014) to our data, which results in

$$\log_{10} \text{SFR}\left(\frac{M_\odot}{\text{yr}}\right) = a + b \log_{10}\left(\frac{M_*}{M_\odot}\right) - c \log_{10}\left(\frac{M_*}{M_\odot}\right)^2, \quad (1)$$

where $a = -24.0415$, $b = 4.1693$, and $c = 0.1638$. To ensure that there was no difference in the SFMS between the edge-on and face-on groups of galaxies, we fit the SFMS again to each of the groups separately, and found that the separate fits have very similar values to those of the total sample. Additionally, we recover the known redshift dependence of the SFMS by fitting the low-redshift and high-redshift samples separately. We find similar results whether we use a redshift-dependent SFMS or an SFMS that is constant with redshift. Therefore, for simplicity, we use the constant SFMS. We divide the sample into two groups of SFR using Equation (1), with one group above and one group below the SFMS.

Finally, because our motivating question is how galaxy inclination affects dust properties, we further divide each of the four bins in the SFR-M_* plane into two equal-sized groups in axis ratio, using the median axis ratio of the sample, $b/a = 0.55$, as a divider. Given that the galaxies are consistent with being disks (see Section 2.5), these two samples roughly correspond to edge-on (which refers to the groups with $b/a < 0.55$, the left panel of Figure 1) and face-on galaxies (referring to $b/a \geqslant 0.55$, the right panel of Figure 1). The edge-on groups have a median $b/a \approx 0.4$, while the face-on groups have a median $b/a \approx 0.7$.

In summary, we have eight groups, where each of the four bins in the SFR-M_* plane are divided into edge-on and face-on axis ratio groups. We note that our results are unaffected by the choice of SFRs for this division. For example, we reach similar conclusions when using spectral energy distribution SFRs rather than Hα SFR. This result is not surprising, as several works have shown that the SFRs agree well (e.g., Steidel et al. 2014; Shivaei et al. 2016; Theios et al. 2019; Price et al. 2020).

3.2. Spectral Stacking

In order to substantially increase the signal-to-noise ratio of the spectra to measure an accurate Balmer decrement for a complete sample of galaxies, we employ spectral stacking within each of the eight groups.

First, we move the spectra of all galaxies to the rest frame and correct for the luminosity distance. As all MOSDEF spectra were flux calibrated, the resulting spectra present the luminosity density. Therefore, stacking in this manner effectively weights the spectra by SFR, as a galaxy with higher SFR will have more flux in its Balmer lines and thus will contribute more to the Balmer decrement of the stack. In essence, this weights the

spectra such that each star-forming region within these galaxies is counted roughly equally. Therefore, studying these stacks gives insight into how dust affects the star-forming regions at high redshift.

To compute a stacked spectrum, we first take the rest-frame spectrum of each galaxy in a group and create a mask to identify sky lines and regions with poor atmospheric transmission. We mask pixels where the measured error is at least 10 times larger than the median measured error of the spectrum. Next, all galaxies must be on the same wavelength axis to perform the stacking, so we linearly interpolate the spectra to 0.5 Å per pixel, which is roughly the dispersion of the spectra in the rest frame. Finally, before stacking, we extend the sky line mask to encompass one additional pixel to either side of the sky lines, as these pixels are far more uncertain due to the interpolation.

With all galaxies on the same wavelength axis and bad pixels masked out, we perform the stacking: at each pixel, we set the value of the stack to the median of all of the nonmasked points contributing to it. Due to the different redshifts of the galaxies, this procedure results in all of the galaxies contributing to the stacks in the regions of 4800–5100 Å and 6400–6700 Å rest frame, but as low as 10% contributing to the regions between these bands, such as 5500 Å. For the purposes of this work, we are interested the emission-line regions, so the larger uncertainties in the regions far from the lines are not relevant. Uncertainties on the spectrum are computed by adding the weighted errors of each contributing point in quadrature.

One concern of this technique is how well the emission lines from galaxies with different velocity dispersions will combine. To assess this potential issue, we generated synthetic Hα and Hβ lines with a realistic range of Balmer decrements (3–6), velocity dispersions (70–150 km s^{-1}), and redshifts (1.6 $\leqslant z \leqslant$ 2.6). Using the same stacking technique that we applied to the data, we stacked these synthetic lines and attempted to recover their mean Balmer decrements, changing several parameters to assess the recovery accuracy. First, increasing the resolution of the spectral interpolation from 0.5 to 0.001 Å had no effect on the recovered Balmer decrements, so the effects of the Nyquist bias seem negligible. Then, we tested smoothing the synthetic emission lines to the same velocity dispersion and observed no effect on the recovered Balmer decrements. In all cases, stacking using the median was better at recovering the sample median Balmer decrement, whereas stacking using the mean typically underestimated the median Balmer decrement by roughly 2%. As a result of these tests, we proceeded with the spectral stacking by taking the median of all pixels that contribute to a given point. However, we also repeated the analysis in this paper with mean stacking, and found similar results that are consistent within the uncertainties.

We also stack the FAST stellar continuum models using the same method that is used for the spectra. We interpolate the models to the same wavelength axis as the spectra. Then, at each point, we take the median of all of the scaled FAST models that contribute to it. These continuum models include Balmer absorption and are therefore necessary for deriving accurate measurements of the Balmer-line fluxes in the stacks.

Since the FAST continuum models were generated from photometry, they need to be scaled to match the spectra. Assuming that the continuum has the correct shape, we compute two scale factors: one for the emission lines near Hα (using 6300 Å $< \lambda <$ 6900 Å), and one for the lines near Hβ
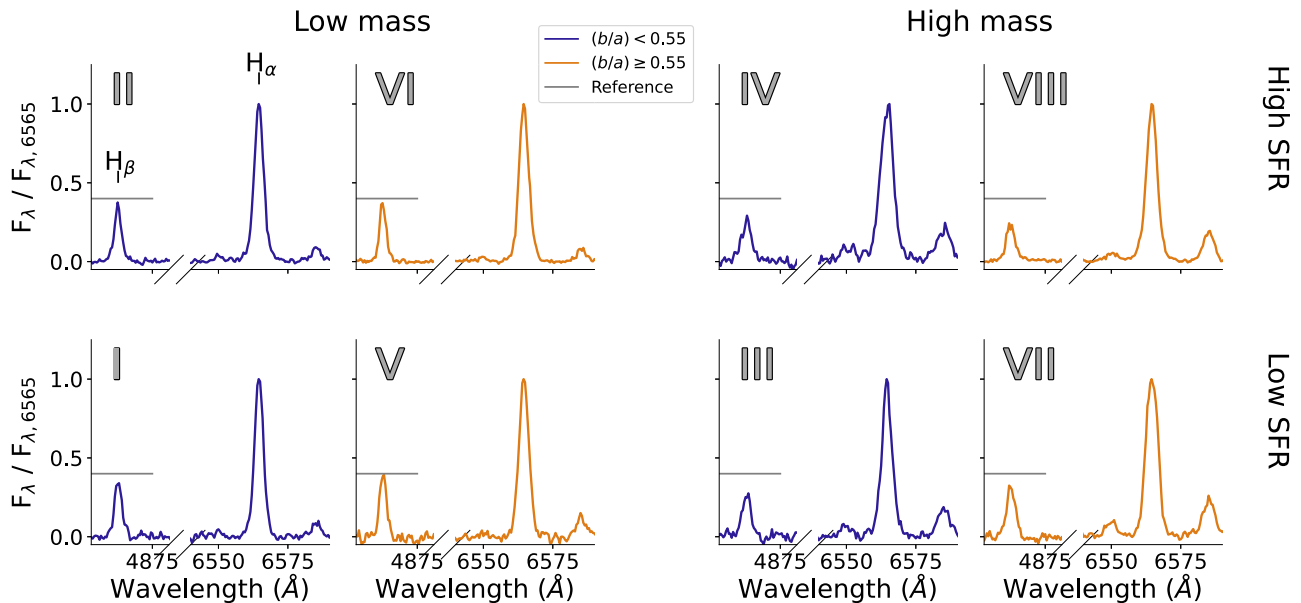
Figure 4. Stacked spectra for the eight groups illustrated in Figure 1. We organize the spectra by stellar mass (left: low mass, right: high mass), SFR (bottom: low SFR, top: high SFR), and axis ratio (blue: edge-on, orange: face-on). The continuum has been subtracted for all stacked spectra. The spectra are normalized so they have the same Hα peak flux for visual comparison. It is visible that the lower-mass galaxies (left) have higher normalized Hβ fluxes than the higher-mass galaxies (right), which results in a smaller Balmer decrement for the lower-mass galaxies. We do not observe a clear change in the Balmer decrement with a changing axis ratio for any of the groups.

(using 4600 Å $< \lambda <$ 5200 Å). When scaling the continuum, we mask out a broad region over the emission lines. Then, in each group, we subtract the scaled continuum model from the spectrum, leaving just the emission lines. We present a subset of the continuum-subtracted Hα and Hβ regions for the stacked spectra in Figure 4.

3.3. Emission Fitting

For each of the stacks, we fit Hβ 4863 Å, [O III] 4960 Å and 5008 Å, Hα 6565 Å, and [N II] 6550 Å and 6585 Å. To first order, the lines are Gaussian, so all six emission lines are fit simultaneously with a Gaussian located at the expected center of each line at a fixed galaxy rotation velocity. We fit for redshift (which should be nearly zero because these are rest frame), velocity dispersion, and the amplitude of each line. With these fluxes, we compute the Balmer decrements and metallicities for each group.

To obtain the uncertainties on all of the emission-line measurements and resulting properties (i.e., Balmer decrement and metallicity), we use bootstrapping. Within each group, we randomly draw n galaxies with replacement, where n is the size of the group. Then we stack their spectra as described in Section 3.2 and repeat this process 100 times. Each of the 100 bootstrapped spectra in each group was fit and integrated with the same method as above, and then a lower and upper 1σ uncertainty was computed as the 16th and 84th percentile of the resulting distribution, respectively.

3.4. Metallicity Measurement

Since the gas-phase metallicity is an important parameter for understanding dust in galaxies, we also measure the metallicities for the eight groups. Not all galaxies in the stacks cover the [O II] 3726–3729 Å doublet, so we are limited in options for our metallicity calibration. Fortunately, we have all the required lines for O3N2, which is one of the more robust calibrators

because it is computed from multiple line ratios and independent of dust effects (e.g., Liu et al. 2008; Steidel et al. 2014; Sanders et al. 2015). Metallicities for the stacks are computed from this O3N2 line ratio, defined as

$$O3N2 = \log_{10}\left(\frac{\text{[O III] } 5008 \text{ Å } / \text{H}\beta}{\text{[N II] } 6585 \text{ Å } / \text{ H}\alpha}\right). \quad (2)$$

We convert the measured O3N2 values into metallicity from the relation described in Bian et al. (2018), derived from observations of galaxies at low redshift that are analogs of high-redshift galaxies. This relation is

$$12 + \log_{10}(\text{O/H}) = 8.97 - 0.39 \times \text{O3N2}. \quad (3)$$

We also measure the metallicities of the 100 bootstrapped spectra in each group, fitting their emission lines and using the same calculation. Uncertainties on the metallicities are then derived from the 16th and 84th percentile of the resulting measured metallicity distribution.

4. Results

With measurements of the eight stacked spectra, each constructed from galaxies that share similar masses, SFRs, and axis ratios, we can now assess the effects of inclination on the dust properties.

First, we examine the relation between dust, as measured by the Balmer decrement, and the mass, SFR, and axis ratios of the groups. In Figure 5 we plot the measured Balmer decrements against median mass, color-coded by the median SFR and shaped by the median axis ratio of the galaxies in the group. Interestingly, edge-on galaxies have the same Balmer decrement as face-on galaxies at fixed mass and SFR. We recover the previously found trend that the Balmer decrement increases with increasing stellar mass (e.g., Garn & Best 2010; Price et al. 2014; Shapley et al. 2022). For the low-mass galaxies, no secondary trends between Balmer decrement and SFR appear.
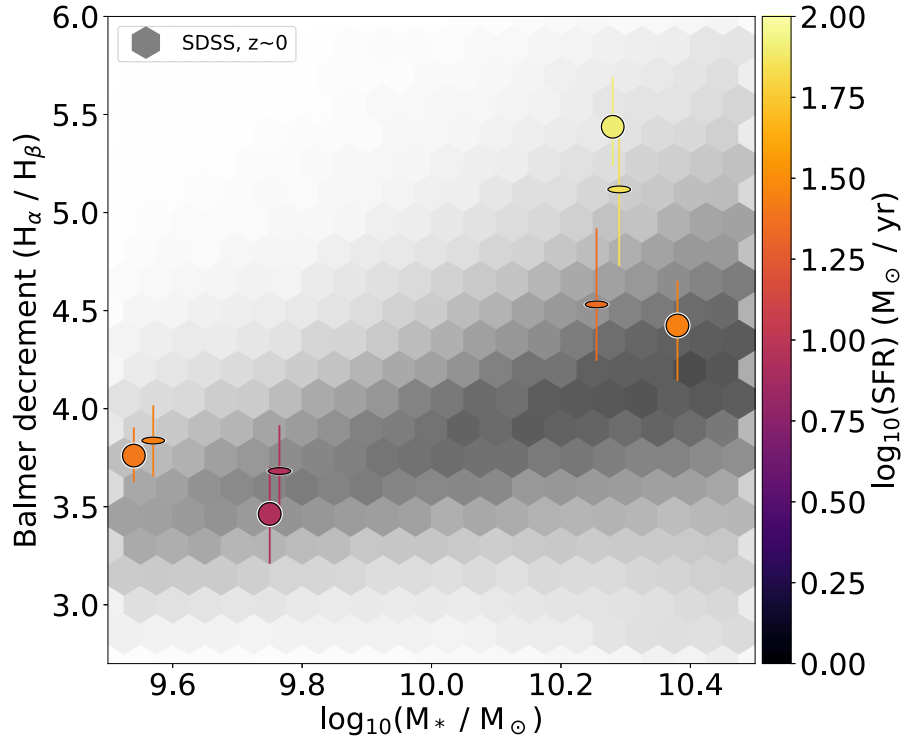
Figure 5. Balmer decrement vs. the median stellar mass in each of the eight groups, color-coded by SFR, with the Balmer decrement of low-redshift SDSS galaxies shown in the gray background hexagons. Flat colored symbols show edge-on galaxies ($b/a < 0.55$), while colored circles show face-on galaxies ($b/a \geqslant 0.55$). Edge-on galaxies have the same Balmer decrement as face-on galaxies at fixed mass and SFR in this sample. Consistent with previous findings, a clear trend with mass is visible, where higher-mass galaxies have higher Balmer decrements (e.g., Garn & Best 2010; Shapley et al. 2022). No strong residual trends appear with the axis ratio or SFR for low-mass galaxies. At high mass, galaxies with higher SFR have slightly higher Balmer decrements.
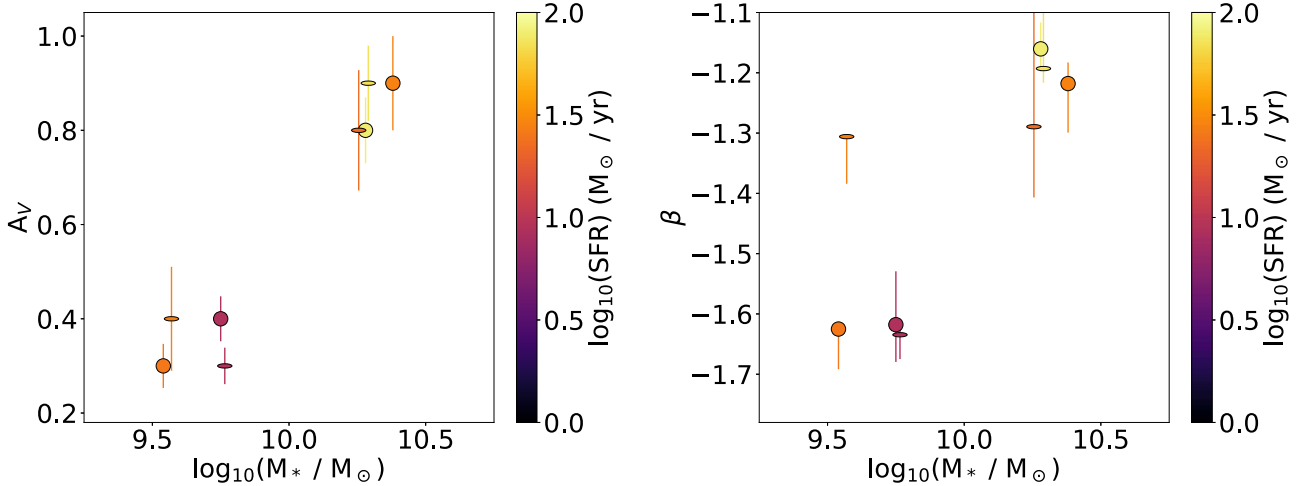
Figure 6. Attenuation in the V band vs. stellar mass (left) and UV slope (β) vs. stellar mass (right). Both A_V and β are measured as the median of the fits to the SEDs of the individual galaxies in each group. A_V and β appear to be similar for edge-on and face-on galaxies at fixed mass and SFR. We see a strong correlation in both A_V and β with mass, but no residual trends with the axis ratio or SFR.

However, at high mass, higher SFR leads to a slightly higher Balmer decrement.

Each galaxy also has a measured attenuation in the V band (A_V) and UV slope (β) from the best-fit stellar population model to their SED (see Section 2.1). For each of the groups, we plot the median A_V and β values versus stellar mass, colored by the SFR and shaped by the axis ratio in Figure 6. Again, the dust properties of edge-on and face-on galaxies in our sample appear to be similar at fixed mass and SFR. We observe a strong trend of increasing dust content with increasing mass.

There is no apparent secondary dependence on SFR or axis ratio.

We also investigate the relation between the attenuation of the Balmer lines and the attenuation of the stellar continuum. The difference between these values, calculated in the V band, is displayed in Figure 7 as a function of stellar mass. Consistent with our previous results, there is no correlation with inclination. However, we do observe that galaxies with higher mass and SFR have increasingly more attenuation in the Balmer lines than the stellar continuum, which places an

Table 1
For Each of the Eight Groups, We Display Our Measured Values of the Stellar Mass, SFR, Axis Ratio, Redshift, Metallicity, A_V, β, and the Balmer Decrement

Group	$\overline{\log_{10}(M^*)}(M_\odot)$	$\overline{\log_{10}(\mathrm{SFR})}\ (M_\odot\,\mathrm{yr}^{-1})$	$\overline{\text{Axis Ratio}}$	$\overline{z}$	$12 + \log_{10}(\mathrm{O/H})$	$\overline{A_V}$	$\overline{\beta}$	$(\mathrm{H}\alpha/\mathrm{H}\beta)$
I	9.77	0.96	0.38	2.2	$8.36\pm^{0.03}_{0.03}$	0.3 ± 0.04	$-1.63\pm^{0.05}_{0.04}$	$3.68\pm^{0.23}_{0.2}$
II	9.57	1.44	0.41	2.23	$8.32\pm^{0.05}_{0.0}$	0.4 ± 0.12	$-1.31\pm^{0.0}_{0.08}$	$3.84\pm^{0.18}_{0.18}$
III	10.26	1.35	0.42	1.92	$8.61\pm^{0.0}_{0.03}$	0.8 ± 0.12	$-1.29\pm^{0.24}_{0.12}$	$4.53\pm^{0.39}_{0.29}$
IV	10.29	1.84	0.42	2.23	$8.55\pm^{0.02}_{0.01}$	0.9 ± 0.08	$-1.19\pm^{0.11}_{0.02}$	$5.12\pm^{0.38}_{0.39}$
V	9.75	0.94	0.69	2.11	$8.44\pm^{0.03}_{0.03}$	0.4 ± 0.05	$-1.62\pm^{0.06}_{0.05}$	$3.46\pm^{0.24}_{0.25}$
VI	9.54	1.41	0.72	2.2	$8.31\pm^{0.02}_{0.01}$	0.3 ± 0.06	$-1.63\pm^{0.03}_{0.05}$	$3.76\pm^{0.14}_{0.14}$
VII	10.38	1.45	0.7	2.18	$8.68\pm^{0.0}_{0.04}$	0.9 ± 0.13	$-1.22\pm^{0.03}_{0.11}$	$4.42\pm^{0.23}_{0.28}$
VIII	10.28	1.9	0.71	2.27	$8.58\pm^{0.01}_{0.01}$	0.8 ± 0.07	$-1.16\pm^{0.04}_{0.07}$	$5.44\pm^{0.25}_{0.2}$

Note. A bar over the symbol denotes that the property is the median of the constituent galaxies in a group.
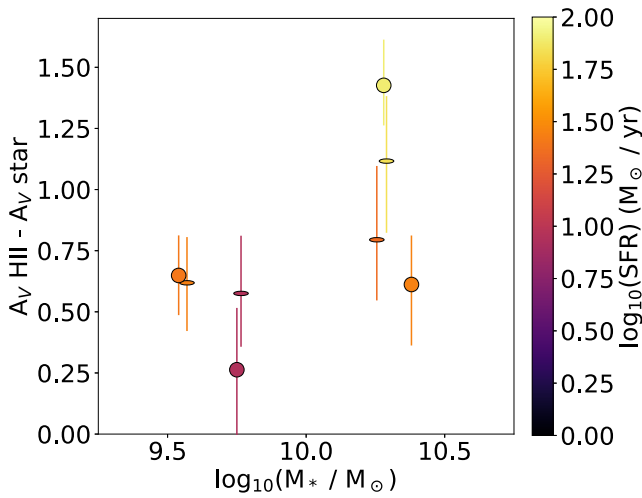
Figure 7. The difference in attenuation between the Balmer lines and stellar continuum, measured in the V band, plotted against stellar mass. Again, we see no effects with inclination. We also observe that galaxies with higher mass and SFR tend to have higher excess nebular attenuation than galaxies at lower masses.

additional constraint on the dust geometry (see Section 5.1). Similar results of an increasing Balmer attenuation relative to the continuum with increasing mass are observed in for distant star-forming galaxies by Price et al. (2014) and Reddy et al. (2020).

To further search for any trends with axis ratio, we plot all galaxies in each group in a UVJ diagram (Figure 8), separated by mass and SFR. The UVJ diagram is a useful diagnostic because more dusty galaxies tend to be located toward the upper right corner of the diagram (e.g., Patel et al. 2012). Within each mass and SFR bin, the distributions for low and high axis ratio galaxies are similar. The lack of visible trends with axis ratio in the UVJ diagram further confirms our results of no trend between dust properties and galaxy inclination. Again, we recover a strong trend with mass, where the higher-mass galaxies tend to be at higher values of both U-V and V-J, indicating higher dust attenuation (e.g., Labbé et al. 2005; Brammer et al. 2009; Williams et al. 2009).

In summary, we observe no trends between the Balmer decrement, A_V, β, and UVJ diagram position with the axis ratio. We conclude that the dust properties appear to be independent of the axis ratio in the regime of redshift, mass, and SFR probed by the MOSDEF survey. We also find that the

Balmer decrement, A_V, and β increase with increasing galaxy mass. Additionally, there is more nebular attenuation than stellar attenuation, and this difference grows larger with increasing galaxy mass and SFR. A table of our measured values for the mass, SFR, axis ratio, and dust properties is displayed as Table 1.

5. Discussion

In this section, we propose explanations for why the Balmer decrement, A_V, and β do not depend on the galaxy axis ratio and what this implies for the dust geometry (Section 5.1). We then compare this work to previous studies (Section 5.2). Finally, we demonstrate why at fixed mass the Balmer decrement might exhibit no secondary dependence on SFR or metallicity, as seen in the low-mass galaxies in our sample (Section 5.3).

5.1. Implications for the Dust-to-Star Geometry

The optical depth of dust depends on the opacity and density of the obscuring material, as well as on the path length of the light through the galaxy. Thus, we may expect that dust attenuation would correlate with the axis ratio, as the light from more edge-on galaxies may encounter more obscuring material. However, we find that the Balmer decrement does not depend on the inclination, implying that light from the youngest stars in observed edge-on, and face-on galaxies encounter the same amount of obscuration.

Interestingly, similar to the Balmer decrement, A_V and β do not change with inclination either. A_V and β measure the attenuation toward all stars, not just the young stellar population. Typically, the older stellar population is only attenuated by the diffuse ISM, as older stars are no longer in star-forming regions. Thus, we would expect to see a clear dependence of A_V and β on the axis ratio. Our finding that there is no trend of the Balmer decrement, A_V, or β with axis ratio seems to contradict any model in which ISM dust plays a large role in attenuation. For example, the two-component model mentioned in the introduction does not appear to hold, as it predicts a substantial ISM dust component, which would lead to inclination-dependent attenuation. However, the galaxies in our sample have relatively high sSFRs, even below the star-forming main sequence ($-9.0 < \log_{10}(\mathrm{sSFR}\ \mathrm{yr}^{-1}) < -8.1$). Therefore, a substantial fraction of the stellar continuum light from these galaxies may be emitted from young stars in star-forming regions rather than from the older stellar populations, and ISM dust might not significantly attenuate the stellar light.
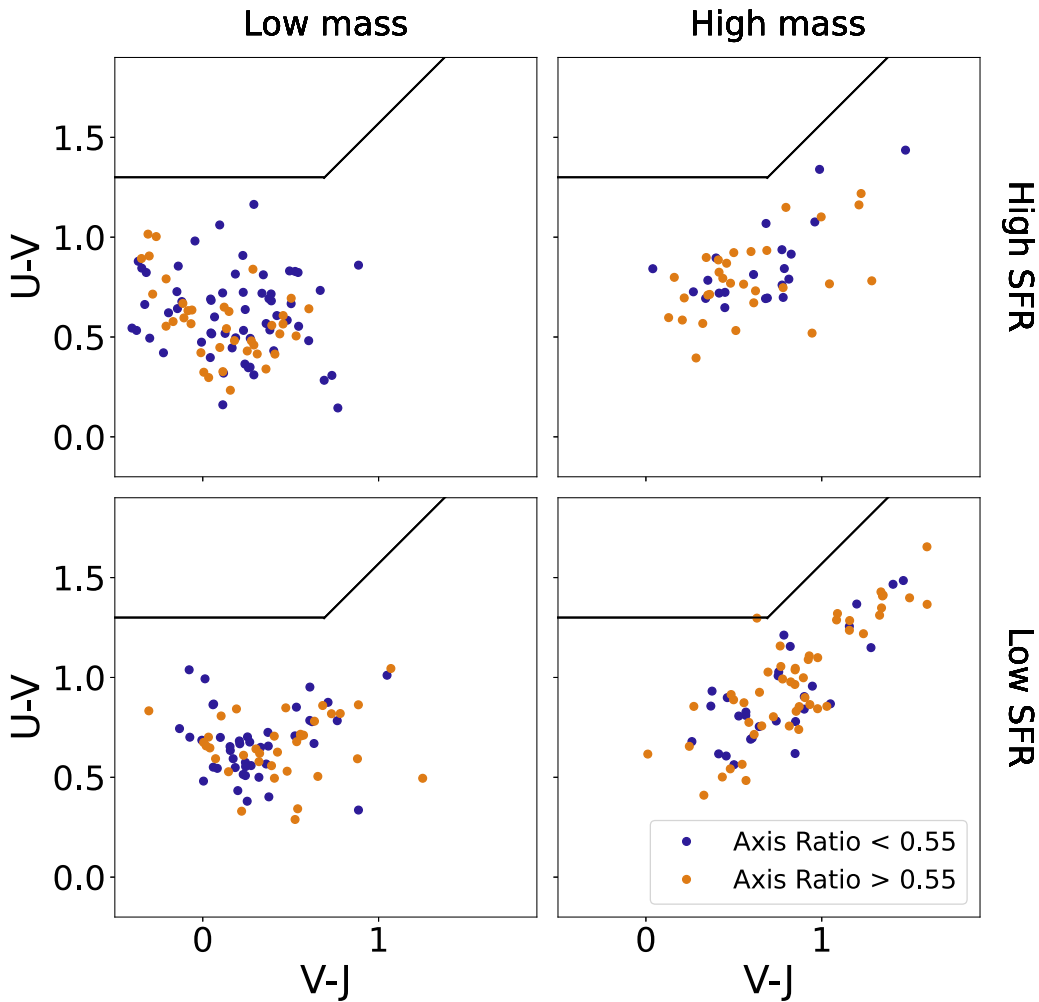
Figure 8. The UVJ diagram for each of the eight groups, organized by stellar mass (left: low mass, and right: high mass), SFR (bottom: low SFR, and top: high SFR), and axis ratio (blue: edge-on, and orange: face-on). All points fall in the region of star-forming galaxies in the diagram. Galaxies with more dust tend to be located toward the upper right corner of the diagram (e.g., Patel et al. 2012). Within each group, the distribution of points is similar, indicating that there is no correlation between dust and axis ratio. By comparing the groups, we see that the high-mass galaxies appear to have higher *U-V* and *V-J*, which is consistent with the hypothesis that high-mass galaxies are more dusty.

For a dust model to be consistent with our results, the model must be able to explain the following findings:

1. Dust attenuation for both the Balmer lines and stellar continuum does not depend strongly on inclination (Figures 5, 6).
2. The total amount of attenuation in the Balmer lines and in the continuum increases with galaxy mass (Figures 5, 6).
3. The Balmer lines are increasingly more attenuated than the continuum as galaxy mass and SFR increase (Figure 7).

Based on these constraints, we propose a dust model in which attenuation occurs in three main components: large star-forming clumps, typical star-forming regions, and a very small amount from the ISM (see also Reddy et al. 2020). This model is similar to the two-component model that was found to be valid at low redshift, with the addition of large, dusty, star-forming clumps.

Large star-forming clumps are indeed observed in galaxies at $z \sim 2$ in Hα and in rest-frame UV maps. These large, 1 kpc scale structures can contribute up to 20% of the star formation in the galaxy (Schreiber et al. 2011; Wuyts et al. 2012).

Moreover, as galaxy mass increases, the clumps tend to be larger (Swinbank et al. 2012) and more common (Tadaki et al. 2014). As they are detected through Hα, these clumps are a strong source of Balmer emission.

Our dust model meets all of the constraints imposed by the data. First, to meet the constraint of independence from inclination effects, the ISM is not a large contributor to attenuation in our model. The observed galaxies have high sSFRs, which causes a significant fraction of the stellar light to be coming form star-forming regions rather than from the older population. Then, because most attenuation occurs in (roughly spherically symmetric) star-forming regions and clumps, changes in attenuation with inclination would not be observed (constraint 1). Second, clumps are larger and more common as galaxy mass increases. Since these clumps emit a fraction of the blue stellar light, as well as a large amount of Balmer emission, the average path length of the light increases with mass for both the continuum and Balmer lines (constraint 2). Third, Balmer attenuation is dominated by clumps, while stellar attenuation primarily probes the less obscured, typical, star-forming regions. Thus, the model predicts that the Balmer attenuation will exceed the continuum attenuation because clumps are more dusty. Then, as galaxy mass and SFR increase, the clump

Top View
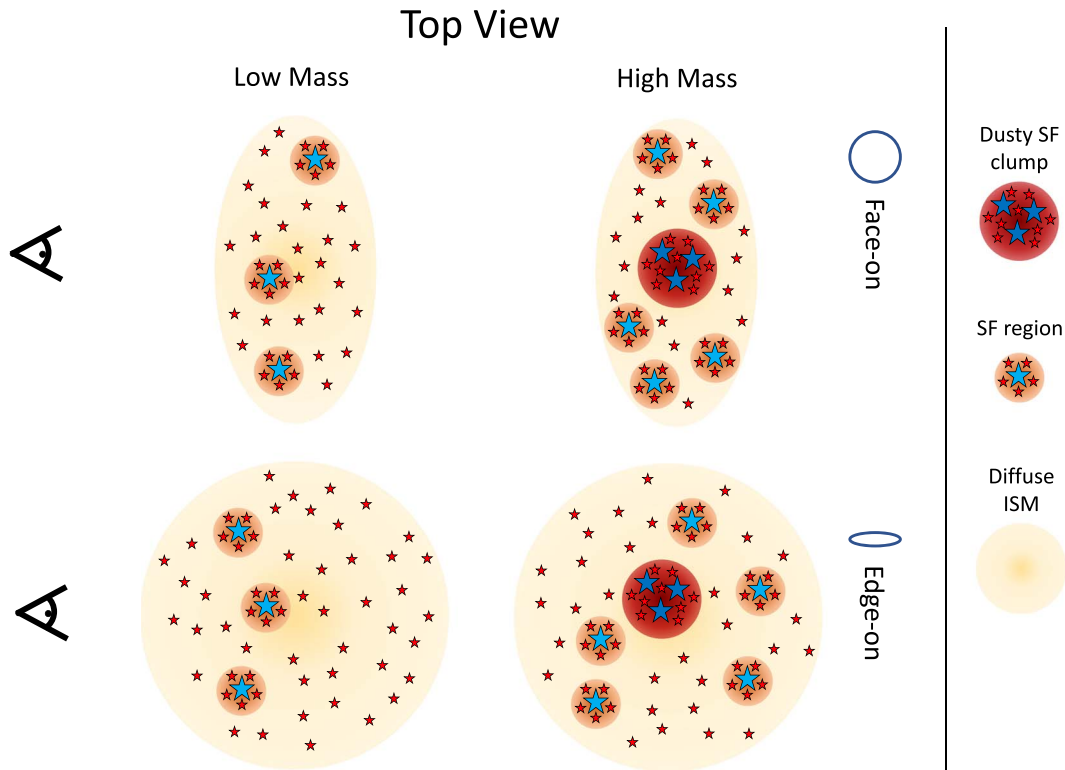
Figure 9. One low-mass galaxy (left) and one high-mass galaxy (right) viewed by an observer as a face-on (top) and edge-on (bottom) system. The observer is represented by an eye, and the reader views the picture from above. The yellow background represents dust in the diffuse ISM, orange represents dust in typical-size star-forming regions, and red represents dust in the large 1 kpc scale star-forming clumps. Both of the star-forming structures are populated with young stars, but there is a higher fraction of young stars in the clumps. In all cases, because the ISM does not contribute much to the attenuation, the observer sees similar attenuation in the face-on and edge-on orientations. Moreover, at higher masses (right), higher attenuation is observed due to the longer average path length of light through the larger clumps. Finally, the excess attenuation ($A_{\text{Balmer}} - A_V$) is higher for the high-mass (high SFR) galaxies because the additional Balmer light originates in the massive clumps.

size and prevalence increases, and so the model predicts an increasing difference between the Balmer and stellar attenuation (constraint 3). Our model meets all constraints of the data, and is presented pictorially in Figure 9.

A different explanation for our results might be that dusty star formation in these galaxies is concentrated toward the center, perhaps in a bulge-like structure. There are some indications for this in high-redshift galaxies, where ALMA observations detected high central infrared SFRs in high-mass galaxies at $z = 2.5$ (e.g., Barro et al. 2016). If the dominant source of the Balmer emission and attenuation is centrally located and occurs in a structure that is roughly spherical, then the encountered dust column density might not change substantially with inclination (constraint 1). In this central star formation model, larger galaxies have larger regions of central star formation, and thus a longer path length through attenuating material to escape (constraint 2). Finally, to explain the higher differential attenuation between the Balmer lines and continuum emission, the youngest stars must be formed closer to the center, while other star-forming regions might be located farther out. As the galaxy mass increases, the fraction of star formation from the dusty central starburst increases, and thus the nebular attenuation increases faster than the stellar attenuation (constraint 3).

Finally, it is expected that scattering of thermal emission in the disk of edge-on galaxies would lead to radiation loss in directions perpendicular to the disk (Misiriotis et al. 2001). We note that for our sample, we do not observe any difference in MIPS 24 micron emission between edge-on and face-on

galaxies with similar properties. Although the MIPS 24 micron band does not probe thermal emission well because it is in the regime of polycyclic aromatic hydrocarbons, this result points to the fact that the energy balance is similar for both orientations. The reason that we do not see any difference may again be the high sSFR of our sample, which might cause most dust obscuration to occur in spherically symmetric regions. If indeed dust spread throughout the whole disk does not play a large role in scattering thermal emission, there would not be an expected trend with the axis ratio.

In the future, our proposed geometry can be tested with dust measurements of individual galaxies across the full range of axis ratios and SFRs, as well as in further investigations of the distribution of star formation and clumps in high-redshift galaxies.

5.2. Comparison to Other Studies

Our data support a geometry in which attenuating dust is mostly concentrated around star-forming regions and clumps, explaining the observations that the Balmer decrement does not vary with axis ratio. The ISM does not seem to play a large role in attenuation, especially due to the relatively high sSFR of the galaxies. Our findings fit the framework suggested by Reddy et al. (2020), in which young star-forming regions may be dustier and contribute strongly to nebular attenuation. Our observations also partially agree with the patchy dust model proposed by Reddy et al. (2015), according to which the youngest stars become increasingly more obscured as the SFR

increases. However, this model is not fully consistent with our observations because it also predicts that the stellar attenuation is dominated by the more diffuse ISM dust, and thus we would expect to see a trend between the axis ratio and A_V or β. Another patchy dust model is presented in Fetherolf et al. (2023), in which the dust transitions from smooth to patchy as galaxy mass increases, and dusty clumps are predicted at high masses. This model is consistent with our results as long as the ISM dust does not cause much of the observed stellar attenuation.

The lack of any Balmer decrement correlation with axis ratio is consistent with Yip et al. (2010), Battisti et al. (2017), and Yuan et al. (2021), who all found analogous results for samples at similar stellar masses at low redshift, and consequently lower SFR. Yip et al. (2010) and Yuan et al. (2021) observed that the stellar continuum attenuation is higher in low-redshift edge-on galaxies than in face-on galaxies. Nonetheless, they concluded that dust attenuation primarily takes place in H II regions and that attenuation in the ISM of the thick disk is insignificant, similar to our results. Our results also contradict Patel et al. (2012) at lower redshift ($0.6 < z < 0.9$), who found that galaxies with higher $V - J$ values have lower axis ratios. Similar results were found by Zuckerman et al. (2021), who showed that the wide range of dust attenuation values measured for star-forming galaxies at a given redshift and stellar mass is almost entirely due to the effect of inclination. This result is mostly valid for $z < 1.5$, but it is less apparent at higher redshifts. These inconsistencies may be partly explained by the lower sSFR at later times, as less stellar light would originate from star-forming regions. Furthermore, there may be more ISM dust at lower redshifts. Indeed, at $z \approx 1.4$ and at lower sSFRs than in this work, Price et al. (2014) demonstrated a relation between the sSFR and the difference between nebular and stellar attenuation for star-forming galaxies in the 3D-HST survey.

5.3. Explaining why the Balmer Decrement Primarily Depends on Mass

In Section 4 we found that the Balmer decrement is independent of the SFR at fixed stellar mass for the low-mass galaxies and shows only a minor dependence on SFR for the more massive galaxies. This result may seem puzzling because galaxies with higher SFRs at fixed mass have higher gas fractions (e.g., Kennicutt 1998), and thus may be expected to have more dust. The amount of dust in a galaxy is connected to the amount of gas through the gas-phase metallicity. Thus, in order to explain our results, the next natural step is to investigate the metallicities of our galaxies.

In Figure 10 we show that the median mass of each group and the measured metallicity (from stacked spectra) recovers the well-known mass–metallicity relation (Tremonti et al. 2004): higher-mass galaxies have higher gravitational potentials, so they retain more metals. Figure 10 also shows that we recover the fundamental metallicity relation (FMR; Mannucci et al. 2010): a higher SFR leads to lower metallicity at fixed mass. This anticorrelation between the SFR and metallicity is thought to arise because high SFR tends to be indicative of a high inflow of metal-poor gas from the intergalactic medium (IGM), and vice versa. We refer to Sanders et al. (2015, 2018, 2020, 2021) for detailed studies of the FMR in the MOSDEF survey.
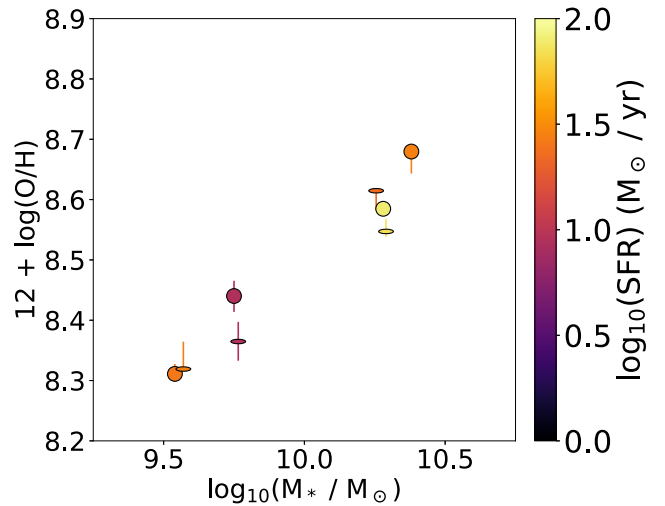

Figure 10. Gas-phase metallicity computed from O3N2 plotted against stellar mass for each of the eight groups. The points are colored by SFR. The measured metallicities show a clear mass–metallicity relation, as expected. At similar stellar mass, a higher SFR leads to a lower metallicity, also as expected.

Since the Balmer decrement increases with mass, we might expect from the mass–metallicity relation that the Balmer decrement would also increase with metallicity. While this trend holds at a large-scale level, our data reveal that the Balmer attenuation does not strongly depend on the metallicity at fixed mass. The left panel of Figure 11 shows that one value of the Balmer attenuation (calculated directly from the Balmer decrement, as in Price et al. 2014) corresponds to a wide range of metallicities for low-mass galaxies, spanning 0.2 dex. At high mass, there seems to be a trend in the opposite direction than expected, where higher metallicities exhibit lower Balmer decrements. Similarly, we show that there is no correlation between the Balmer attenuation and SFR for the low-mass galaxies (Figure 11, right panel).

Our results of a roughly constant Balmer attenuation at constant mass imply that these galaxies, despite the range in SFRs and metallicities, must have approximately the same dust column density. Fundamentally, this arises from the following argument. Assuming a fixed metal yield, the amount of metals in a galaxy only depends on the total mass that has been formed. Since dust is formed from metals, we expect that the dust column density (and thus the Balmer decrement) similarly only depends on the galaxy mass. On the other hand, because the metallicity is defined with respect to the hydrogen content, the metallicity depends on both the dust column density and the gas column density. For example, adding more low-metallicity gas (i.e., infalling from the IGM) will not change the dust column density, but it will lower the metallicity. Therefore, we find a range of metallicities at fixed Balmer decrement due to changes in the gas fraction.

Another way to understand the result that the Balmer decrement only depends on stellar mass is to use the observed relations to examine the interplay between the SFR and metallicity. To compare these properties, we consider both the FMR and the Kennicutt–Schmidt (K-S) relation (Kennicutt 1998). These relations together indeed provide a qualitative explanation for how a wide range of SFRs and metallicities can have the same Balmer attenuation. The K-S relation states that at fixed mass, galaxies with a higher SFR will have a higher hydrogen gas content, fueled by infalling IGM gas. This IGM
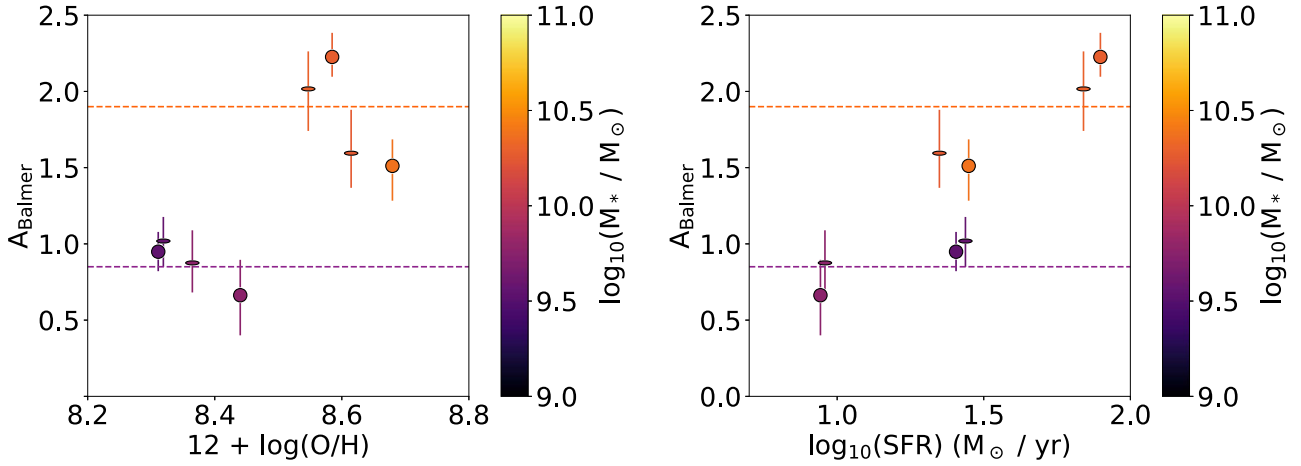
Figure 11. Balmer attenuation vs. metallicity (left) and vs. SFR (right), colored by the median stellar mass. We show dashed lines of the average Balmer attenuation for the four low-mass (purple) and four high-mass (orange) groups. At a similar Balmer attenuation and stellar mass, we observe a wide range of SFRs and metallicities for the low-mass galaxies. At high mass, there appears to be a small trend where the Balmer attenuation decreases with increasing metallicity, and increases with increasing SFR. We conclude that the Balmer attenuation primarily depends on stellar mass for the low-mass galaxies in our sample.

gas is metal poor, resulting in a decrease in the metallicity as the SFR increases—this relation is the FMR. By definition, a low metallicity implies a low dust-to-gas ratio. Therefore, galaxies with higher SFRs have more gas, but a lower dust-to-gas ratio, and thus can have the same dust column density as galaxies with low SFRs and consequently high dust-to-gas ratios. The relation between metallicity, SFR, and the Balmer decrement is shown in the diagram of Figure 12.

To assess whether these different relations indeed lead to a range of SFRs and metallicities at fixed Balmer decrement, we now explore this model quantitatively. As supported by our results, we assume a dust geometry that does not depend on inclination (e.g., Section 5.1). We assume that this attenuating dust has a dust mass absorption coefficient, κ_λ, which is spatially independent and that the dust is spread evenly throughout the attenuating region (either typical star-forming regions or dusty star-forming clumps). From these two assumptions, Shapley et al. (2022) derived that the dust attenuation is proportional to the dust-to-gas ratio and gas surface density,

$$A_\lambda \approx 1.086 \times \kappa_\lambda \times \left(\frac{M_{\mathrm{dust}}}{M_{\mathrm{gas}}}\right) \times \Sigma_{\mathrm{gas}}. \tag{4}$$

We can replace $(M_{\mathrm{dust}}/M_{\mathrm{gas}})$ using the power-law relation from De Vis et al. (2019), which is

$$\log_{10}\left(\frac{M_{\mathrm{dust}}}{M_{\mathrm{gas}}}\right) = a \times [12 + \log_{10}(\mathrm{O/H})] + b. \tag{5}$$

Empirically, they find $a \approx 2.15$ for the O3N2 metallicity calibration, and we can fold b into our constants. We also note that there does not appear to be significant evolution in the dust-to-gas ratio from $z = 0$ to $z \approx 2$, so this relation is applicable (Shapley et al. 2020; Popping et al. 2023). We can use the K-S relation (Kennicutt 1998) to replace Σ_{gas} from Equation (4), given by

$$\Sigma_{\mathrm{gas}} \propto (\Sigma_{\mathrm{SFR}})^{(\frac{1}{n})}. \tag{6}$$
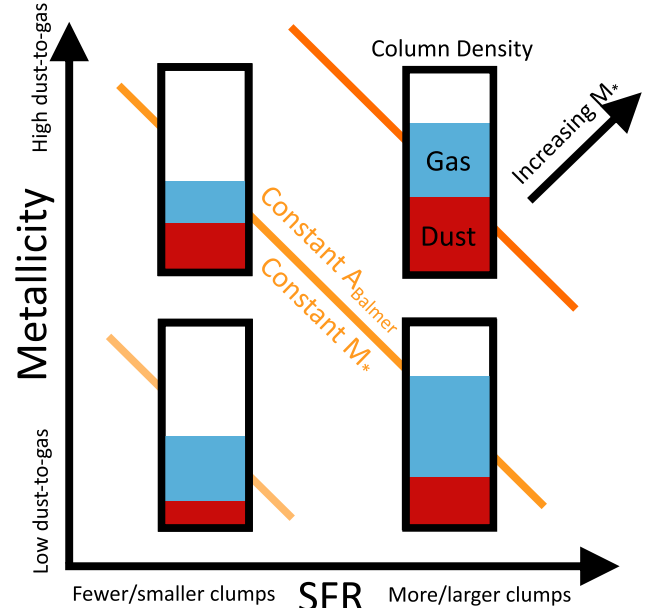

Figure 12. Diagram depicting how the relation between the SFR and the metallicity affects the Balmer attenuation. The bars represent the column density of gas (blue) and dust (red) encountered by escaping light for the galaxies that fall in the corresponding parts of the SFR-metallicity plane. The lines of roughly constant A_{Balmer} (from Equation (8)) and constant mass (from the FMR) are shown in the background in orange. Galaxies at a higher SFR (right) have more star-forming clumps, so the light sees a longer path length of gas and dust on average. Galaxies with higher metallicities (top) have higher dust-to-gas ratios, so a larger fraction of their gas column density is filled with obscuring dust. This representation shows that galaxies with the same dust column density (i.e., top left and bottom right) and thus the same Balmer attenuation can have very different metallicities and SFRs.

We now replace Σ_{SFR} with its definition, focusing specifically on the attenuating region, which is

$$\Sigma_{\mathrm{SFR}} = \frac{\mathrm{SFR}}{2\pi R_{\mathrm{sf}}^2}. \tag{7}$$

Here, R_{sf} is the effective size of all of the star-forming regions and clumps. Since nearly all of star formation in these galaxies
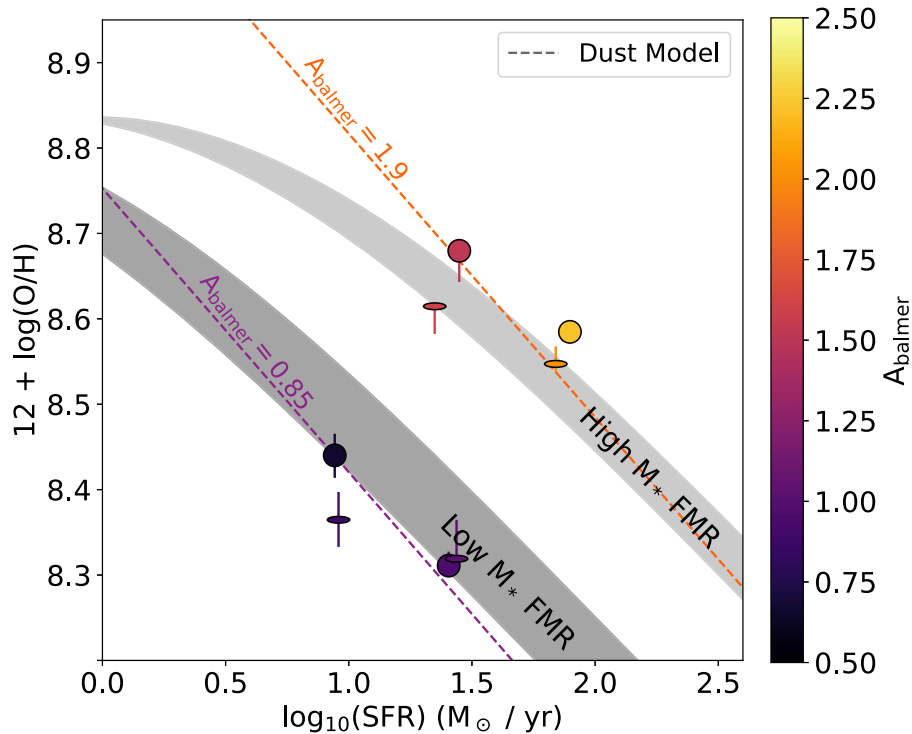
Figure 13. Metallicity vs. SFR for the eight groups of galaxies, color-coded by stellar mass. We show the lines of constant Balmer attenuation generated from our dust model (Equation (8), adopting $a = 2.15$, $n = 1.4$ and leaving R_{sf} free). Additionally, we display the shaded regions of the FMR from Sanders et al. (2021), which correspond to the mean masses of the low- and high-mass groups. The groups appear to fall near the lines of constant attenuation despite their differing metallicities and SFRs. The slope of constant Balmer attenuation appears to be very similar to the slope of the FMR at fixed mass, so galaxies of similar mass will have a similar Balmer attenuation, regardless of their SFR or their corresponding metallicity.

takes place in star-forming regions and clumps, the numerator of the K-S relation is the global SFR of the galaxy. Substituting everything into Equation (4), we arrive at

$$A_\lambda \propto 10^{a \times [12 + \log_{10}(O/H)]} \times \left(\frac{SFR}{R_{sf}^2} \right)^{\left(\frac{1}{n} \right)}. \qquad (8)$$

Therefore, we find that the Balmer attenuation, A_{Balmer}, should be higher with increasing metallicity (higher dust-to-gas ratio), increasing SFR (more gas in the galaxy), and decreasing R_{sf} (more gas per unit area). Finally, this gives a prediction for the relation between metallicity and SFR that can control the Balmer attenuation. At fixed mass, if the metallicity decreases linearly with $\log_{10}(SFR)$, we would find a constant Balmer attenuation.

Coincidentally, the FMR does indeed show that the metallicity decreases roughly linearly with $\log_{10}(SFR)$. To illustrate the relation between the FMR and our dust model, we plot our model, along with our measured SFRs, metallicities, and the FMR, in Figure 13. We fix a constant of proportionality and solve for the best-fitting R_{sf} using least squares for the low- and high-mass galaxies separately. The FMR is from Sanders et al. (2021) for MOSDEF $z \approx 2.3$ and $z \approx 3.3$ star-forming galaxies. This relation is

$$12 + \log_{10}(O/H) = 8.80 + 0.188y - 0.220y^2 - 0.0531y^3, \qquad (9)$$

where $y = \mu_{0.60} - 10$ and $\mu_{0.60} = \log(M_*/M_\odot) - 0.6 \times \log(SFR/M_\odot \ yr^{-1})$.

Figure 13 shows that the groups divide clearly by mass, each falling on their own roughly linear relation between the metallicity and SFR, as dictated by the FMR from Sanders et al. (2021). We also see the lines of constant Balmer attenuation as predicted by our model in Equation (8). Most notably, we find that the slope of the FMR at fixed mass (≈ -0.25) is very similar to the slope of a constant Balmer attenuation according to the model (-0.33). Therefore, at fixed mass, any SFR has a corresponding metallicity from the FMR that results in a constant Balmer decrement. This correlation implies that the galaxy mass is the only driver of the Balmer attenuation, which is highlighted in the diagram in Figure 12.

Finally, we note that for either of the proposed dust geometries from Section 5.1, this dust model can still hold. Although the dust may be distributed among star-forming regions and clumps, the attenuating dust is roughly spherically symmetric. The assumptions for this model require only a uniform dust distribution and a spatially independent κ_λ, which are both plausible.

6. Summary

In this paper, we use a sample of 308 star-forming galaxies at $1.37 \leqslant z \leqslant 2.61$ from the MOSDEF survey to assess the relation between the dust properties and galaxy inclination. The galaxies have stellar masses of $9 \leqslant \log(M_*) \leqslant 11$ and measured axis ratios from deep HST/CANDELS imaging. We divide the data into eight groups such that within each group, the galaxies have a similar SFR, stellar mass, and axis ratio. In each group, we stack the spectra of all constituent galaxies. From these stacks, we measure the emission lines to determine the Balmer decrements and metallicities. We also compute the

median A_V and β for each group. Below, we summarize our key findings.

1. All 308 galaxies have axis ratio measurements, with similar measurements in both F125W and F160W. Based on the distribution of these axis ratios, this sample of MOSDEF galaxies appears to be disky.

2. The Balmer decrement, as well as A_V and β, is independent of galaxy inclination. We do not find trends in the UVJ distribution with inclination either. Thus, face-on and edge-on galaxies have the same dust attenuation in our sample.

3. The Balmer decrement, A_V, and β all increase with increasing galaxy mass. Especially for the low-mass galaxies, the Balmer decrement seems to be primarily determined by the galaxy stellar mass, with no residual dependence on the SFR or the metallicity. The high-mass galaxies may show a slight trend of an increasing Balmer decrement with increasing SFR.

4. The nebular attenuation is higher than the stellar attenuation, and this difference grows even larger at higher masses and SFRs. This finding implies that the nebular emission originates from more dusty regions than the stellar emission on average, and the prevalence of these dustier regions increases with the galaxy mass and SFR.

5. The lack of variation in the Balmer decrement, A_V, and β with galaxy inclination supports a geometry in which the diffuse ISM does not play a large role in attenuation. We propose a three-component model consisting of very dusty and large star-forming clumps, typical star-forming regions, and minimal contributions from the diffuse ISM. In this model, the dust attenuation does not show changes with inclination because the attenuation primarily occurs in (roughly spherical) star-forming regions and clumps. Due to the low dust content in the ISM and the high sSFR of the sample, we expect that both the nebular and stellar attenuation are independent of inclination. This model also predicts the trend that the nebular and stellar attenuation increases with galaxy mass because the clumps are larger and more prevalent at higher galaxy masses. Finally, because more nebular emission originates from the clumps and the clumps emit a larger fraction of the light at higher galaxy masses, the model also explains the growing differential attenuation between the nebular and stellar components as galaxy mass increases (see also Reddy et al. (2020)).

6. A fixed metal yield naturally explains why the Balmer decrement solely depends on galaxy mass, with no residual dependence between the Balmer decrement and the SFR or the metallicity. The Balmer decrement only depends upon the dust column density, while the SFR and the metallicity relate to the gas content. Another way to understand this result is by examining the relation between the gas content (related to the SFR by the K-S relation) and the dust-to-gas ratio (related to metallicity) of a galaxy. At fixed mass, a galaxy with a higher SFR will have a lower metallicity (i.e., the FMR), resulting in the same Balmer decrement as in a galaxy with a low SFR, but a higher metallicity. Equation (8) describes this relation quantitatively.

The work above is based on stacked spectra. While stacking spectra is an incredibly powerful tool, it comes with some limitations. For example, rather than probing a continuous range of SFRs, we are only able to probe two bins—information is washed out in the stacks. Rather than averaging over so many properties, we ideally would like to have accurate dust properties, SFR, mass, and axis-ratio measurements for each individual galaxy. In particular, with these measurements, we could check the lowest sSFR galaxies to determine whether the A_V and β properties change with the axis ratio, as we expect from our work. Similarly, examining the systems with the lowest axis ratios to search for increased dust attenuation would give more insight into the role of the diffuse ISM in dust attenuation. Neither of these tests are possible with the current data because the signal-to-noise ratio of the emission features to measure the Balmer decrements and metallicities are too low.
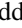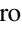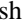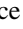
With higher-quality data on each galaxy, we would no longer need to stack the spectra, and therefore could obtain an even more accurate picture of the distribution of dust in star-forming galaxies during the epoch of peak star formation in the universe. Fortunately, with the James Webb Space Telescope (JWST), it will finally be possible to obtain such spectroscopic samples and probe the dust distributions of high-redshift galaxies in detail. Additionally, with the NIRSpec integral field unit on JWST, it will be possible to directly test our proposed three-component model. It can obtain Balmer decrements directly from the large star-forming clumps and from the regions around them to verify that the clumps indeed cause stronger attenuation.

ORCID iDs

Brian Lorenz ⓘ https://orcid.org/0000-0002-5337-5856
Mariska Kriek ⓘ https://orcid.org/0000-0002-7613-9872
Alice E. Shapley ⓘ https://orcid.org/0000-0003-3509-4855
Naveen A. Reddy ⓘ https://orcid.org/0000-0001-9687-4973
Ryan L. Sanders ⓘ https://orcid.org/0000-0003-4792-9119
Guillermo Barro ⓘ https://orcid.org/0000-0001-6813-875X
Alison L. Coil ⓘ https://orcid.org/0000-0002-2583-5894
Bahram Mobasher ⓘ https://orcid.org/0000-0001-5846-4404
Sedona H. Price ⓘ https://orcid.org/0000-0002-0108-4176

Jordan N. Runco ⓘ https://orcid.org/0000-0003-4852-8958
Irene Shivaei ⓘ https://orcid.org/0000-0003-4702-7561
Brian Siana ⓘ https://orcid.org/0000-0002-4935-9511
Daniel R. Weisz ⓘ https://orcid.org/0000-0002-6442-6030

References

Azadi, M., Coil, A. L., Aird, J., et al. 2017, ApJ, 835, 27
Barro, G., Kriek, M., Pérez-González, P. G., et al. 2016, ApJL, 827, L32
Battisti, A. J., Calzetti, D., & Chary, R.-R. 2017, ApJ, 851, 90
Bian, F., Kewley, L. J., & Dopita, M. A. 2018, ApJ, 859, 175
Brammer, G. B., van Dokkum, P. G., Franx, M., et al. 2012, ApJS, 200, 13
Brammer, G. B., Whitaker, K. E., van Dokkum, P. G., et al. 2009, ApJL, 706, L173
Calzetti, D., Armus, L., Bohlin, R. C., et al. 2000, ApJ, 533, 682
Cardelli, J. A., Clayton, G. C., & Mathis, J. S. 1989, ApJ, 345, 245
Chabrier, G. 2003, PASP, 115, 763
Charlot, S., & Fall, S. M. 2000, ApJ, 539, 718
Coil, A. L., Aird, J., Reddy, N., et al. 2015, ApJ, 801, 35
Conroy, C., & Gunn, J. E. 2010, ApJ, 712, 833
Conroy, C., Gunn, J. E., & White, M. 2009, ApJ, 699, 486
De Vis, P., Jones, A., Viaene, S., et al. 2019, A&A, 623, A5
Elmegreen, B. G., & Elmegreen, D. M. 2006, ApJ, 650, 644
Faber, S. 2011, The Cosmic Assembly Near-IR Deep Extragalactic Legacy Survey ("CANDELS"), Mikulski Archive for Space Telescopes, doi:10.17909/T94S3X
Fetherolf, T., Reddy, N. A., Shapley, A. E., et al. 2023, MNRAS, 518, 4214
Garn, T., & Best, P. N. 2010, MNRAS, 409, 421
Genzel, R., Burkert, A., Bouché, N., et al. 2008, ApJ, 687, 59
Grogin, N. A., Kocevski, D. D., Faber, S. M., et al. 2011, ApJS, 197, 35
Hao, C.-N., Kennicutt, R. C., Johnson, B. D., et al. 2011, ApJ, 741, 124
Kennicutt, R. C., Jr+ 1998, ApJ, 498, 541
Koekemoer, A. M., Faber, S. M., Ferguson, H. C., et al. 2011, ApJS, 197, 36
Kriek, M., Shapley, A. E., Reddy, N. A., et al. 2015, ApJS, 218, 15
Kriek, M., van Dokkum, P. G., Labbé, I., et al. 2009, ApJ, 700, 221
Labbé, I., Huang, J., Franx, M., et al. 2005, ApJL, 624, L81
Lambas, D. G., Maddox, S. J., & Loveday, J. 1992, MNRAS, 258, 404
Liu, X., Shapley, A. E., Coil, A. L., Brinchmann, J., & Ma, C.-P. 2008, ApJ, 678, 758
Mannucci, F., Cresci, G., Maiolino, R., Marconi, A., & Gnerucci, A. 2010, MNRAS, 408, 2115

McLean, I. S., Steidel, C. C., Epps, H. W., et al. 2012, Proc. SPIE, 8446, 84460J
Misiriotis, A., Popescu, C. C., Tuffs, R., & Kylafis, N. D. 2001, A&A, 372, 775
Momcheva, I. G., Brammer, G. B., van Dokkum, P. G., et al. 2016, ApJS, 225, 27
Patel, S. G., Holden, B. P., Kelson, D. D., et al. 2012, ApJL, 748, L27
Peng, C. Y., Ho, L. C., Impey, C. D., & Rix, H.-W. 2010, AJ, 139, 2097
Popping, G., Shivaei, I., Sanders, R. L., et al. 2023, A&A, 670, A138
Price, S. H., Kriek, M., Barro, G., et al. 2020, ApJ, 894, 91
Price, S. H., Kriek, M., Brammer, G. B., et al. 2014, ApJ, 788, 86
Price, S. H., Kriek, M., Shapley, A. E., et al. 2016, ApJ, 819, 80
Reddy, N. A., Kriek, M., Shapley, A. E., et al. 2015, ApJ, 806, 259
Reddy, N. A., Shapley, A. E., Kriek, M., et al. 2020, ApJ, 902, 123
Rodríguez, S., & Padilla, N. D. 2013, MNRAS, 434, 2153
Salim, S., & Narayanan, D. 2020, ARA&A, 58, 529
Sanders, R. L., Shapley, A. E., Jones, T., et al. 2021, ApJ, 914, 19
Sanders, R. L., Shapley, A. E., Kriek, M., et al. 2015, ApJ, 799, 138
Sanders, R. L., Shapley, A. E., Kriek, M., et al. 2018, ApJ, 858, 99
Sanders, R. L., Shapley, A. E., Reddy, N. A., et al. 2020, MNRAS, 491, 1427
Schreiber, N. M. F., Shapley, A. E., Genzel, R., et al. 2011, ApJ, 739, 45
Shapley, A. E., Cullen, F., Dunlop, J. S., et al. 2020, ApJL, 903, L16
Shapley, A. E., & Sanders, R. L., Salim, S., et al. 2022, ApJ, 926, 145
Shivaei, I., Kriek, M., Reddy, N. A., et al. 2016, ApJL, 820, L23
Shivaei, I., Reddy, N. A., Shapley, A. E., et al. 2015, ApJ, 815, 98
Simons, R. C., Kassin, S. A., Weiner, B. J., et al. 2017, ApJ, 843, 46
Skelton, R. E., Whitaker, K. E., Momcheva, I. G., et al. 2014, ApJS, 214, 24
Steidel, C. C., Rudie, G. C., Strom, A. L., et al. 2014, ApJ, 795, 165
Swinbank, A. M., Smail, I., Sobral, D., et al. 2012, ApJ, 760, 130
Tadaki, K.-i., Kodama, T., Tanaka, I., et al. 2014, ApJ, 780, 77
Theios, R. L., Steidel, C. C., Strom, A. L., et al. 2019, ApJ, 871, 128
Tremonti, C. A., Heckman, T. M., Kauffmann, G., et al. 2004, ApJ, 613, 898
van der Wel, A., Bell, E. F., Häussler, B., et al. 2012, ApJS, 203, 24
Whitaker, K. E., Franx, M., Leja, J., et al. 2014, ApJ, 795, 104
Wild, V., Charlot, S., Brinchmann, J., et al. 2011, MNRAS, 417, 1760
Williams, R. J., Quadri, R. F., Franx, M., van Dokkum, P., & Labbé, I. 2009, ApJ, 691, 1879
Wuyts, S., Labbé, I., Franx, M., et al. 2007, ApJ, 655, 51
Wuyts, S., Schreiber, N. M. F., Genzel, R., et al. 2012, ApJ, 753, 114
Yip, C.-W., Szalay, A. S., Wyse, R. F. G., et al. 2010, ApJ, 709, 780
Yuan, F.-T., Lu, J., Shen, S., & Boquien, M. 2021, ApJ, 911, 145
Zuckerman, L. D., Belli, S., Leja, J., & Tacchella, S. 2021, ApJL, 922, L32